Impact of Nb vacancies and p-type doping of the NbCoSn-NbCoSb half-Heusler thermoelectrics

PCCP

Accepted Manuscript

This article can be cited before page numbers have been issued, to do this please use: D. A. Ferluccio, R. Smith, J. Buckman and J. Bos, *Phys. Chem. Chem. Phys.*, 2018, DOI: 10.1039/C7CP07521A.

ROYAL SOCIETY OF CHEMISTRY

rsc.li/pccp

View Article Online
DOI: 10.1039/C7CP07521A

Impact of Nb vacancies and p-type doping of the NbCoSn-NbCoSb half-Heusler thermoelectrics

Daniella A. Ferluccio,[a] Ronald I. Smith[b], Jim. Buckman[c] and Jan-Willem G. Bos[a*]

[a] *Institute of Chemical Sciences and Centre for Advanced Energy Storage and Recovery, School of Engineering and Physical Sciences, Heriot-Watt University, Edinburgh, EH14 4AS, UK.*

[b] *ISIS Facility, Rutherford Appleton Laboratory, Harwell Oxford, Didcot, OX11 0QX, UK.*

[c] *Institute of Petroleum Engineering, Heriot-Watt University, Edinburgh, EH14 4AS, UK.*

* j.w.g.bos@hw.ac.uk

The half-Heuslers NbCoSn and NbCoSb have promising thermoelectric properties. Here, an investigation of the $NbCo_{1+y}Sn_{1-z}Sb_z$ (y = 0, 0.05; $0 \leq z \leq 1$) solid-solution is presented. In addition, the p-type doping of NbCoSn using Ti and Zr substitution is investigated. Rietveld analysis reveals the gradual creation of Nb vacancies to compensate for the n-type doping caused by the substitution of Sb in NbCoSn. This leads to a similar valence electron count (~18.25) for the $NbCo_{1+y}Sn_{1-z}Sb_z$ samples ($z > 0$). The mass fluctuation disorder due to the Nb vacancies strongly decreases the lattice thermal conductivity from 10 W m^{-1} K^{-1} (z = 0) to 4.5 W m^{-1} K^{-1} (z = 0.5, 1). This is accompanied by a transition to degenerate semiconducting behaviour leading to large power factors, S^2/ρ = 2.5-3 mW m^{-1} K^{-2} and figures of merit, ZT = 0.25-0.33 at 773 K. Ti and Zr can be used to achieve positive Seebeck values, e.g. S = +150 μV K^{-1} for 20% Zr at 773 K. However, the electrical resistivity, ρ_{323K} = 27-35 mΩ cm, remains too large for these materials to be considered useful p-type materials.

Introduction

Reducing the reliance on fossil fuels requires the development of sustainable methods for energy production as well as improvements in energy efficiency. Thermoelectric power generation is

View Article Online
DOI: 10.1039/C7CP07521A

one method that has gained interest for the conversion of waste heat into electricity.[1] The thermoelectric efficiency of a material is given by its figure of merit, $ZT = (S^2/\rho\kappa)T$, where S is the Seebeck coefficient, ρ is the electrical resistivity, κ is the thermal conductivity and T is the absolute temperature.[1] A large $ZT \geq 1$ is desirable for optimum performance, however, it is not possible to optimise the individual parameters independently, and developing efficient thermoelectric materials remains challenging.[1, 2]

Half-Heuslers (HHs) are one class of semiconducting compounds that have been extensively investigated in recent years, due to their desirable thermoelectric properties, thermal stability and synthesis from earth-abundant elements.[3-6] HH thermoelectrics have the general formula XYZ, where X and Y are usually transitions metals and Z is a main group element, crystallising in the $F\bar{4}3m$ space group with an 18 valence electron count (VEC), which leads to semiconducting properties. HHs have good electrical properties but are limited by their high lattice thermal conductivities, leading to the identification of several routes to reduce this parameter, including alloying,[7-9] grain size reduction[10, 11] and nanocomposite formation.[12-14] The best performing n- and p-type HH compositions have $ZT \geq 1$ at elevated temperatures and are based on XNiSn (X = Ti, Zr, Hf)[8, 15-18] and XCoSb or NbFeSb,[11, 19-21] respectively.

NbCoSn is another possible 18 VEC composition that has recently attracted renewed interest with the report of large power factors $S^2/\rho = 3.5$ mW m^{-1} K^{-2} and $ZT = 0.6$ at 1000 K in n-type $NbCoSn_{1-z}Sb_z$ ($z \leq 0.15$) compositions.[22] These enhanced properties, compared to the previous best ZT = 0.2-0.3 values,[23-25] were attributed to an improved sample purity achieved through an arc-melting, ball-milling and hot-pressing procedure. While n-type doping is relatively easy to achieve using Sb,[22-24] p-type doping of NbCoSn has proved more difficult. Kawaharada *et al.* reported that Ti and Hf are weak p-type dopants with a low Seebeck coefficient.[26, 27] By contrast, recent computational work suggests that Ti, Zr and Hf should be strong p-type dopants.[28] The p-type doping of NbCoSn is of significant interest as bandstructure calculations indicate a favourable electronic structure with multiple valence band maxima

View Article Online
DOI: 10.1039/C7CP07521A

contributing to the electronic transport.[22] Addition of a second $NbCo_2Sn$ full-Heusler phase has been reported to enhance the properties of NbCoSn but the S^2/ρ of these samples remains low (< 1 mW m^{-1} K^{-2}).[29] The related compound NbCoSb was unexpectedly found to exhibit good thermoelectric performance (ZT = 0.4 at 1000 K) despite having a 19 VEC normally associated with metallic HH compositions.[30] A subsequent experimental and computational study revealed that these compositions are in fact Nb deficient with an approximate 18.2 VEC.[31]

Here, we report an investigation of the structures and thermoelectric properties of the full solid-solution between NbCoSn and NbCoSb. In addition, we reinvestigate the use of Ti and Zr as p-type dopants and find that these enable positive Seebeck values but are limited by a large electrical resistivity.

Experimental

Synthesis: Polycrystalline $Nb_{0.8}A_{0.2}Co_{1+y}Sn$ and $NbCo_{1+y}Sn_{1-z}Sb_z$ samples (A = Ti, Zr; $0 \leq y \leq 0.05$; $0 \leq z \leq 1$) were synthesised by direct reaction of elemental powders. All reagents were purchased from Alfa Aesar and have ≥99.8% purity. The Nb, Ti, Zr, Sn powders were 325-mesh; Co <1.6μm and powdered 1-5 mm Sb shots were used. The precursors were mixed using a mortar and pestle according to the target stoichiometries. All reactions were carried out on a 5-gram scale. The mixed powders were cold pressed into 13 mm diameter disks, wrapped in 0.025 mm thickness Ta or Nb foil (Alfa Aesar) and heated at 1073 K for 24 hours inside evacuated quartz tubes. Subsequently, the samples were re-homogenised using a mortar and pestle, cold-pressed and sintered at 1123 K for a further 168 hours. The first heating step used ramping and cooling rates of 10 K/min and 20 K/min, respectively. In the second step, the samples were placed directly into the furnace at 1123 K and air quenched. After sintering, the samples were powdered using a mortar and pestle and consolidated into 13 mm disks by hot pressing under an Argon atmosphere at 1273 K and 80 MPa for 30 minutes.

View Article Online
DOI: 10.1039/C7CP07521A

Characterisation: Laboratory X-ray powder diffraction (XRD) data were collected using a D8 Bruker Advance diffractometer with monochromated Cu $K\alpha_1$ radiation. Rietveld quality datasets were collected over 7 hours. Time-of-flight neutron powder diffraction (NPD) data was collected on the POLARIS instrument at the ISIS facility, Rutherford Appleton Laboratory, UK. 1-2g of powdered hot-pressed samples were loaded into cylindrical vanadium cans and data was collected at room temperature for between 200-300 μAh integrated proton beam current to the ISIS target each (corresponding to approximately 1.5-2 hours exposure to the neutron beam). Rietveld analysis of the X-ray and neutron powder diffraction patterns was done using the GSAS and EXPGUI software.[32, 33]

Microscopy: Scanning electron microscopy and elemental mapping were done using a Quanta 650 FEG SEM operated at 20 kV and equipped with an energy dispersive X-ray spectroscopy (EDX) Oxford Instruments X-max^N 150 mm detector. Prior to analysis, the samples were polished using fine Al_2O_3 sandpaper down to 0.3-micron roughness.

Thermoelectric Property Measurements: The Seebeck coefficient (S) and electrical resistivity (ρ) were measured on bars cut from the hot-pressed samples using a Linseis LSR 3 instrument. The thermal diffusivities (α) of the samples were measured using a Linseis LFA 1000 Laser Flash Apparatus on disks of ~13 mm diameter and ~ 1.5 mm thickness. Discs were coated with graphite spray to avoid emissivity errors. The densities (d) of the samples were calculated from the mass and dimensions of the hot-pressed pellets, and were found to be >90% in all cases. The thermal conductivity $\kappa = \alpha C d$ was calculated using the experimental α and d values and heat capacity data (C) from the literature.[22] A porosity correction; $\kappa/\kappa_{dense} = 1-(4/3)\phi$; $\phi = (100-\%\text{density})/100$ was applied.

Results

Sample preparation and X-ray powder diffraction: Samples were initially prepared by wrapping the cold-pressed pellets in Ta foil. This resulted in the presence of a Ta-based impurity with main

View Article Online
DOI: 10.1039/C7CP07521A

peaks at 2θ = 23°, 2θ = 28° and 2θ = 29° in the XRD patterns (Fig. S1). In addition, these samples contained Nb_3Sn, Co_7Nb_6, Nb_3Sb and Nb_5Sb_4 secondary phases (Fig. S1). These initial reactions also indicated that the use of 5% excess Co (y = 0.05) improved the sample purity for the $NbCo_{1+y}Sn_{1-z}Sb_z$ samples, in agreement with previous literature reports.[25] Addition of excess Co did not improve the purity of the p-type $Nb_{0.8}A_{0.2}Co_{1.05}Sn$ samples. To eliminate the Ta impurity, Nb foil was used during sintering. This strongly reduced the amount of secondary phases present in the XRD data, yielding very good sample purities (Fig. 1). For example, stoichiometric NbCoSn only contains a small amount of a $NbCo_2Sn$ FH phase, while $NbCo_{1.05}Sn$ is free of FH but contains a trace amount of Nb_3Sn (Fig. 1a). This suggests that phase pure NbCoSn can be obtained by further adjustment of the amount of excess Co. The phase purity of the $Nb_{0.8}A_{0.2}CoSn$ samples was also improved by using Nb foil (Fig. 1a). The A = Zr sample has broadened HH reflections that are caused by a shoulder on the low-2θ side, which is indicative of poor mixing of Nb and Zr leading to HH phases with slightly different lattice parameters.[9, 34] The reflections for the A = Ti sample are sharp (Fig. 1a) consistent with the presence of a single HH phase with uniform composition. The only observed impurities in the $NbCo_{1+y}Sn_{1-z}Sb_z$ samples are small amounts of Nb_3Sn and Nb_3Sb (Fig. 1b), where y = 0.05 was found to give the best purities across the whole z range ($0 \leq z \leq 1$).

Lattice parameters were extracted using Rietveld analysis of the XRD data. The values for the samples prepared using Nb foil are summarized in Table 1, while those for the samples prepared with Ta foil are given in Table S1. The refined lattice parameters of both sets of samples are very similar. This indicates that the main impact of the Nb foil is a reduction in the amount of secondary phases but does not lead to compositional changes of the HH phase. The introduction of Ti and Zr leads to a significant increase in HH lattice parameter (Δa = 0.02-0.04 Å). The metallic radii for Ti and Nb are nearly identical (1.46-1.47 Å), while the radius of Zr (1.60 Å) is substantially larger.[35] This suggests that the observed increase in lattice parameter is at least partly electronic in origin and caused by the depopulation of bonding electronic states

View Article Online
DOI: 10.1039/C7CP07521A

upon p-type doping. For the $NbCo_{1.05}Sn_{1-z}Sb_z$ samples a strong reduction in lattice parameter is observed, which we show below is due to the introduction of Nb vacancies on the X site in the HH structure.

Neutron powder diffraction: Neutron powder diffraction (NPD) data were collected from the samples prepared using Ta foil. This was done as these samples were available at the time of the ISIS experiment. As noted above, the main impact of the use of Nb foil is to increase the sample purity, while the HH cell metrics are unchanged. The crystal structure results in this section are therefore valid for the samples on which the thermoelectric measurements were undertaken. The final Rietveld fit for $NbCo_{1.05}Sb$ is shown in Fig. 2, while the fits for the other compositions can be found in Figs. S2 and S3. The lattice, atomic parameters, sample purities and fit statistics are given in Table 2. Comparison of the $NbCo_{1+y}Sn$ samples confirms the improved purity with an increase in HH weight fraction from 89% (y = 0) to 98% (y = 0.05). Refinement of the atomic site occupancies did not suggest any deviation from the ideal NbCoSn stoichiometry in either case, confirming that the HH composition is not affected by the introduction of excess Co, and it is only the sample purity that is improved (Table 1). Refinement of the X-site occupancy for the A = Ti sample yielded an experimental Ti occupancy of 0.13(1), demonstrating that a large amount of Ti has successfully substituted on the X-site. The nearly identical neutron scattering lengths for Zr (b = 7.16 fm) and Nb (b = 7.05 fm) prevented a similar analysis for the A = Zr sample. The A = Zr sample was fitted using two HH phases to account of the observed shoulder at the low d-spacing side (Fig. S2(d)). These phases have fitted lattice parameters of 5.9936(1) Å and 5.9607(2) Å with weight fractions of 77% and 15%, respectively, with the remaining 8% due to impurity phases (Table 2). As indicated above, the presence of multiple HH phases is indicative of the poor mixing of Nb and Zr.

The lattice parameters and refined Nb site occupancies for the $NbCo_{1+y}Sn_{1-z}Sb_z$ series are shown in Fig. 3. Both show a linear decrease with the amount of Sb (z) contained in the samples. The lattice parameter decreases from 5.95 Å (z = 0) to 5.90 Å (z = 1), while the Nb fractional site

View Article Online
DOI: 10.1039/C7CP07521A

occupancy decreases from 1 (z = 0) to 0.86 (z = 1). The linear decrease of the lattice parameter and linear increase in the amount of Nb vacancies evidences a systematic change in the crystal structure, which is likely driven by the desire to keep an optimal VEC near the semiconducting value of 18. The VECs for the $NbCo_{1+y}Sn_{1-z}Sb_z$ series were calculated from the fitted compositions and are shown in the inset to Fig. 3a. The calculated values fall between 18.0-18.5 and are centred on a VEC of 18.25, in good agreement with VEC ~ 18.2 reported for z = 1 in Ref. 31.

Scanning Electron Microscopy: The $NbCo_{1.05}Sn_{0.5}Sb_{0.5}$ sample (prepared using Nb foil), corresponding to the midway point between NbCoSn and NbCoSb was investigated using SEM and EDX elemental mapping. The results are shown in Fig. 4. The backscattered electron (BSE) image reveals contrast variations due to changes in average atomic number (Fig. 4a). These are confirmed by the composite and individual elemental maps (Fig. 4b, c-f). Most of the sample consists of a homogenous HH phase, while two types of secondary phases are evident. The compositions of these phases were determined by averaging at least 4 areas of similar appearance. This revealed an average composition of $Nb_{0.93(1)}CoSn_{0.54(1)}Sb_{0.49(2)}$ for the HH phase, confirming the 7(1)% Nb deficiency also found in NPD (Table 2) and successful substitution of Sb on the Sn site. The estimated standard deviations give an indication of the compositional variation between the selected areas. The red regions, labelled 1, in the composite elemental map were determined to be Nb_3Sb, while the darker green regions generally correspond to Nb_6Co_7. The observation of these secondary phases is in keeping with the Nb deficiency of the HH phase.

Thermoelectric power factor: The temperature dependence of the Seebeck coefficient (S), electrical resistivity (ρ) and power factor (S^2/ρ) for the $NbCo_{1+y}Sn$, $Nb_{0.8}A_{0.2}CoSn$ and $NbCo_{1+y}Sn_{1-z}Sb_z$ samples (all prepared using Nb foil) are shown in Fig. 5. The 323 K thermoelectric properties and maximum power factors are listed in Table 1. A comparison between the $NbCo_{1+y}Sn$ samples is shown in Fig. 5a-c. Both compositions are n-type conductors

View Article Online
DOI: 10.1039/C7CP07521A

with S = -200 μV K^{-1} and ρ = 7.5 mΩ cm (y = 0) and S = -150 μV K^{-1} and ρ = 3.8 mΩ cm (y = 0.05) at 323 K. The reduced S and ρ suggest a small amount of carrier doping has occurred in the y = 0.05 sample. The S(T) show a broad minimum at 500-600 K (Fig. 5b), which is coupled to an increase in ρ(T). The S^2/ρ have a maximum at 500-600 K and peak values of 1.3 mW m^{-1} K^{-2} (y = 0) and 2 mW m^{-1} K^{-2} (y = 0.05).

Substitution of Ti and Zr in NbCoSn results in p-type behaviour with $S_{323\,K}$ = +26 μV K^{-1} (A = Ti) and $S_{323\,K}$ = +42 μV K^{-1} (A = Zr). The ρ(T) values are increased by a factor 4-5 compared to NbCoSn, with ρ_{323K} = 32 mΩ cm (A = Ti) and ρ_{323K} = 27 mΩ cm (A = Zr). The ρ(T) show a semiconductor to semiconductor transition at ~475 K for both samples (Fig. 5d). This is also evident in the S(T), which shows two linear regions with the crossover near 475 K (Fig. 5e). The S(T) for the A = Zr sample increases up to +150 μV K^{-1} at 773 K, while the S(T) for A = Ti remains < 50 μV K^{-1}. The high ρ(T) values lead to low $S^2/\rho \leq 0.1$ mW m^{-1} K^{-2} for the $Nb_{0.8}A_{0.2}Co_{1.05}Sn$ samples (Fig. 5f). The semiconductor-semiconductor transition is unconventional as the drop in ρ(T) is accompanied by an increase in S(T), which goes against the usual dependence on carrier concentration that holds for a single electronic band.[2] As discussed in the introduction, bandstructure calculations for NbCoSn show that several bands can contribute to the carrier transport for p-type samples.[22] A possible explanation for the observed transition is that an additional band contributes at elevated temperatures, leading to a simultaneous increase in S and decrease of ρ as the carriers redistribute. On the other hand, the transition is also evident in κ_{lat} (see below), suggesting that there is a structural component to the transition.

Replacement of Sn by Sb in the $NbCo_{1.05}Sn_{1-z}Sb_z$ series leads to efficient n-type doping (Fig. 5g-i). All samples have a linear ρ(T), characteristic of heavily doped semiconductors, in keeping with the estimated VEC = 18.25 for these samples. At 323 K, ρ ~ 0.3 mΩ cm for z = 0.1, 0.25 and 1, while the midway z = 0.5 sample has a larger ρ = 0.6 mΩ cm (Fig. 5g). The S(T) for

View Article Online
DOI: 10.1039/C7CP07521A

z = 0.1, 0.25 and 1 have similar temperature dependences: a linear increase to ~600 K, above which saturation occurs between -125 μV K^{-1} to -135 μV K^{-1} (Fig. 5h). The z = 0.5 sample has a much more linear S(T) with $S_{773\ K}$ = -120 μV K^{-1}. The S^2/ρ are comparable to the best values in the literature, with $(S^2/\rho)_{max}$ = 3 mW m^{-1} K^{-2} for the z = 0.1 and $(S^2/\rho)_{max}$ = 2.5 mW m^{-1} K^{-2} for z = 1.[22, 30] Due to the saturation of S(T) and the linearly increasing ρ(T) these maximum values are observed at a relatively low temperature of 500-600 K, beyond which S^2/ρ decreases (Fig. 5i).

Thermal conductivity and figure of merit: The temperature dependence of the total thermal conductivity (κ), the lattice thermal conductivity (κ_{lat}) and the thermoelectric figure of merit (ZT) of the $NbCo_{1+y}Sn$, $Nb_{0.8}A_{0.2}CoSn$ and $NbCo_{1+y}Sn_{1-z}Sb_z$ samples (all prepared using Nb foil) are given in Fig. 6. All κ_{lat} follow an approximate T^{-n} dependence, where n falls between 0.3-0.7. This is characteristic of thermal transport limited by point-defect scattering for which n = 0.5, rather than Umklapp scattering, for which n = 1.[36] The 323 K κ_{lat} is ~10 W m^{-1} K^{-1} for NbCoSn and ~8 W m^{-1} K^{-1} for $NbCo_{1.05}Sn$ (Fig. 6b), which is comparable to the values obtained using the directionally solidified (κ_{lat} = 7 W m^{-1} K^{-1} for y = 0.05)[25] and arc-melting and ball milling approaches (κ_{lat} = 8 W m^{-1} K^{-1} for y = 0).[22] The reduced κ and larger S^2/ρ for the y = 0.05 sample produce a performance improvement compared to NbCoSn, resulting in a maximum ZT = 0.2 at 773 K compared to ZT = 0.13 for y = 0 (Fig. 6c). This compares to ZT = 0.25 (y = 0.05) and ZT = 0.2 (y = 0) for the directionally solidified and arc-melting and ball milling approaches.[22, 25]

The large ρ(T) for the $Nb_{0.8}A_{0.2}CoSn$ samples means that κ is almost completely due to κ_{lat} with a negligible Wiedemann Franz (κ_{el}) component (Fig. 6d-e). These samples have $\kappa_{lat,\ 323\ K}$ = 4-5 W m^{-1} K^{-1}, suggesting that alloying on the X-site and the presence of multiple HH phases for the A = Zr sample are efficient in reducing κ_{lat}.[8, 9] The κ(T) also evidence the transition that was observed in S(T) and ρ(T): above 475 K both samples have an additional contribution to κ(T). The shape of this feature mirrors ρ(T) but cannot be explained by an increased κ_{el}, i.e. it remains clearly visible in κ_{lat}(T). The $Nb_{0.8}A_{0.2}CoSn$ samples therefore undergo a transition that impacts

View Article Online
DOI: 10.1039/C7CP07521A

on all thermoelectric parameters. The calculated ZT are smaller than 0.1 (Fig. 6f) due to the poor S^2/ρ for these samples.

The n-type $NbCo_{1.05}Sn_{1-z}Sb_z$ samples show a gradual reduction from κ_{lat} = 8 W m^{-1} K^{-1} at 323 K (z = 0) to κ_{lat} = 4 W m^{-1} K^{-1} for z = 0.5 and κ_{lat} = 5 W m^{-1} K^{-1} for z = 1 (Fig. 6h). The measured value for z = 1 is in good agreement with κ_{lat} = 4.5 W m^{-1} K^{-1} reported for NbCoSb consolidated at the same temperature.[30] The low ρ(T) values lead to large κ_{el} ~ 2 W m^{-1} K^{-1} for z = 0.1, z = 0.25 and z = 1, while the z = 0.5 sample has κ_{el} ~ 1 W m^{-1} K^{-1} (Fig. 6g, h). The non-degenerate z = 0 samples have much lower κ_{el} < 0.2 W m^{-1} K^{-1} (Fig. 6a, b). Despite the differences in S^2/ρ and κ, similar peak ZT = 0.25-0.33 are observed for all samples at 773 K (Fig. 6i). The z = 1 sample has the largest ZT = 0.33, while the z = 0.1 sample has ZT = 0.29 at 773 K.

To help understand the evolution of κ_{lat} of the $NbCo_{1.05}Sn_{1-z}Sb_z$ series, the 323 K data are plotted against the Nb-site vacancy concentration in Fig. 7. This clearly illustrates the gradual reduction of κ_{lat} as the amount of Nb vacancies increases. To link the reduction of κ_{lat} to the crystal structure, the Callaway model was used to assess the impact of the vacancies.[37, 38] This analysis treats the vacancies as atomic point defects causing mass fluctuations, leading to phonon scattering. No other phonon scattering contributions are considered. First, the experimental disorder scattering parameter (Γ_{exp}) was determined using:[38]

$$\frac{\kappa_{lat}}{\kappa_{lat}^{P}} = \frac{\tan^{-1}(u)}{u}, u^2 = \frac{\pi^2 \Theta_D \Omega}{h v^2} \kappa_{lat}^{P} \Gamma_{exp} \quad (1)$$

Here κ_{lat}^{P} is the lattice thermal conductivity of the perfect crystal, u is the disorder scaling parameter, h is Planck's constant, Ω is the average volume per atom, v is the average sound velocity and Θ_D is the Debye temperature. Θ_D was estimated from the average atomic displacement parameter from the NPD fits to the $NbCo_{1+y}Sn$ samples using:[39]

$$U_{iso} = \left[\frac{3h^2}{(m k_B 4\pi^2 \Theta_D^2)}\right] T \quad (2)$$

View Article Online
DOI: 10.1039/C7CP07521A

Here m is the average atomic mass, k_B is Boltzmann's constant, T = 298 K. This resulted in θ_D = 361 K. The velocity of sound was calculated from Θ_D using:

$$v = \frac{\Theta_D 2\pi k_B}{[h(6\pi^2 n)^{1/3}]} \quad (3)$$

Here n is the number of atoms per unit volume (5.8×10^{28} m^{-3} for NbCoSn). This yields an estimated v = 3141 m s^{-1}. Secondly, the theoretical mass fluctuation disorder parameter (Γ_M) was calculated using:[38]

$$\Gamma_M = \frac{1}{3}\, q(1-q)\left(\frac{-m_{Nb}}{m}\right)^2 \quad (4)$$

Here, q is the fraction of Nb-vacancies and m_{Nb} is the mass of a Nb atom. The obtained values are given in Table 3 and increase from Γ_M = 0 for NbCoSn (q = 0) to Γ_M = 0.09 for NbCoSb (q = 0.14). Two sets of Γ_{exp} were determined to reflect the difference in κ_{lat}^P for the $NbCo_{1+y}Sn$ (y = 0, y = 0.05) samples (Fig. 6b). The obtained Γ_{exp} values are listed in Table 3 and show good agreement with the calculated values for Γ_M. For example, the z = 0.5 sample has Γ_{exp} = 0.07-0.08, which is comparable to the theoretical mass fluctuation disorder for 8% Nb vacancies (Γ_M = 0.06). The close agreement between the observed (Γ_{exp}) and theoretical (Γ_M) disorder parameters reveals that the reduction of κ_{lat} can be fully explained by the point defect scattering of phonons, caused by mass fluctuations in the HH structure due to the Nb vacancies.

Discussion

We have investigated the structures and properties of the $NbCo_{1+y}Sn_{1-z}Sb_z$ solid solution whose end-members have attracted interest as promising thermoelectric materials. In addition, we report on attempts at p-type doping NbCoSn. Rietveld analysis of NPD data revealed the introduction of Nb-site vacancies with a linear dependence on Sb content (Fig. 3a). This is driven by the desire to maintain a valence electron count near 18 and agrees with the VEC = 18.2 reported for the z = 1 end member in the literature.[31] No superstructure reflections were observed in

View Article Online
DOI: 10.1039/C7CP07521A

diffraction, consistent with a random arrangement of the Nb vacancies. Rietveld analysis also confirmed that the excess Co used to improve the sample purity does not carry over into the HH structure. The HH compositions are therefore best described as a solid solution between NbCoSn and $Nb_{0.86}CoSb$ (i.e. $Nb_{1-0.14z}CoSn_{1-z}Sb_z$) with a random distribution of Nb and vacancies on the X site. To the best of our knowledge, the presence of stable vacancies on the octahedral X site is rare for semiconducting HH compositions. The data on the $NbCo_{1+y}Sn_{1-z}Sb_z$ solid solution therefore provides an opportunity to study the impact of vacancies on ZT. A clear reduction of κ_{lat} with z is observed. The negligible mass and size differences between Sn and Sb preclude this as a cause for the observed reductions. Instead, the observed reduction from $\kappa_{lat,\ 323K}$ = 8-10 W m^{-1} K^{-1} (z = 0) to 4-5 W m^{-1} K^{-1} (z = 0.5, 1) can be fully explained by the mass fluctuations caused by the presence of the Nb vacancies. This quantitative link confirms that the reduction of κ_{lat} is caused by mass fluctuation induced point defect scattering of phonons, analogous to the well-established impact of alloying. Significantly, the mass fluctuations induced by the Nb vacancies (e.g. Γ_M ~ 0.09 for $Nb_{0.84}CoSb$) are larger than the upper limit for alloying Zr and Hf in ZrNiSn (Γ_M ~ 0.06 for the 50/50 mixture).[38] This demonstrates that vacancies are highly effective in reducing κ_{lat} in HH compounds. However, their application may be limited due to the difficulty in stabilising HHs with X-site vacancies.

The impact of the vacancies on the electrical properties is less clear from the data with no systematic changes in ρ(T) or S(T). This suggests that there are also variations in carrier concentration and that S^2/ρ can be optimised further through chemical doping. Hall measurements would be needed to establish the detailed impact of vacancies on the electrical transport. The largest S^2/ρ for our samples are 3.0 mW m^{-1} K^{-2} (z = 0.1), 2.2 mW m^{-1} K^{-2} (z = 0.25) and 2.5 mW m^{-1} K^{-2} (z = 1). These values are comparable to the best performing NbCoSn and NbCoSb samples prepared via arc melting, ball milling and hot pressing, which have $(S^2/\rho)_{max}$ = 3.4 mW m^{-1} K^{-2} (for $NbCoSn_{0.9}Sb_{0.1}$)[22] and $(S^2/\rho)_{max}$ = 2.2 mW m^{-1} K^{-2} (for

View Article Online
DOI: 10.1039/C7CP07521A

NbCoSb).[30] The thermal conductivities and ZT values for our samples are consistent with the literature with ZT = 0.4 at 773 K for $NbCoSn_{0.9}Sb_{0.1}$ and ZT = 0.3 at 773 K for NbCoSb.[22, 30] The key difference causing the reduced ZT for our z = 0.1 sample is that the S^2/ρ has a broad maximum between 450-600 K, whereas this occurs at higher temperatures, between 600-900 K for the best literature samples, enabling ZT = 0.6.[22] The S^2/ρ plateau is caused by the saturation of S(T) and gradual increase of ρ(T) (Fig. 5g, h). A similar effect is observed for the z = 0 parent material (Fig. 5a, b). This combination of properties is unusual as maxima in S(T) are normally associated with the onset of minority carrier conduction. This should lead to a decrease in ρ(T) and a bipolar contribution to κ(T), which are absent from our data (Figs. 5, 6). A possible explanation is a very low hole mobility, resulting in a small bipolar κ and minor reduction of ρ(T) that is negated by increased carrier scattering at high temperatures. The hypothesis of a low hole mobility is supported by the large ρ(T) values for the p-type $Nb_{0.8}A_{0.2}CoSn$ samples. These high ρ(T) values are hindering attempts to develop these materials as possible p-type thermoelectrics, despite a favourable electronic bandstructure.[22] The presence of the semiconductor-semiconductor transition for the $Nb_{0.8}A_{0.2}CoSn$ samples is another unusual feature of these materials that deserves further investigation.

To conclude, the thermoelectric properties of the $NbCo_{1+y}Sn_{1-z}Sb_z$ and $Nb_{0.8}A_{0.2}CoSn$ (A = Ti, Zr; $0 \le y \le 0.05$; $0 \le z \le 1$) half-Heusler alloys have been investigated. Large power factors S^2/ρ = 2.5-3 mW m^{-1} K^{-2} and ZT = 0.25-0.33 were observed for the $NbCo_{1+y}Sn_{1-z}Sb_z$ series. Rietveld analysis established the presence of Nb vacancies, which occur to maintain a semiconducting electron count near 18.25. The vacancies cause strong mass fluctuations and quantitatively explain the observed reductions in lattice thermal conductivity. The p-type $Nb_{0.8}A_{0.2}CoSn$ samples are limited by high electrical resistivities.

View Article Online
DOI: 10.1039/C7CP07521A

Conflict of interest

There are no conflicts to declare.

Acknowledgements

DAF and JWGB acknowledge the STFC for allocation of neutron scattering beamtime at the ISIS facility (RB1620138), the EPSRC is acknowledged for funding (EP/N01717X/1) and a studentship for DAF.

View Article Online
DOI: 10.1039/C7CP07521A

Table 1. Lattice parameters (a) from X-ray powder diffraction, sample densities, 323 K Seebeck coefficients (S_{323K}), 323 K electrical resistivity (ρ_{323K}), 323 K thermal conductivity (κ_{323K}), maximum power factors ($(S^2/\rho)_{max}$) and maximum ZT (ZT_{max}) values for the $NbCo_{1+y}Sn$ (y = 0, 0.05), $Nb_{0.8}A_{0.2}CoSn$ (A = Ti, Zr) and $NbCo_{1.05}Sn_{1-z}Sb_z$ ($0 \leq z \leq 1$) samples synthesised using Nb foil.

Composition	*a* (Å)	Density (g/cm^3)	S_{323K} ($\mu V\ K^{-1}$)	P_{323K} ($m\Omega\ cm$)	κ_{323K} ($W\ m^{-1}\ K^{-1}$)	$(S^2/\rho)_{max}$ ($mW\ m^{-1}\ K^{-2}$)	ZT_{max}
NbCoSn	5.9526(1)	8.1	-202	7.4	9.9	1.3	0.14
$NbCo_{1.05}Sn$	5.9538(1)	8.8	-148	3.8	8.1	2.0	0.21
$Nb_{0.8}Ti_{0.2}CoSn$	5.9706(3)	8.4	26	32.4	4.7	0.009	0.002
$Nb_{0.8}Zr_{0.2}CoSn$	5.9920(1)	8.4	43	26.9	4.0	0.1	0.03
$NbCo_{1.05}Sn_{0.9}Sb_{0.1}$	5.9527(2)	8.4	-84	0.3	8.8	2.9	0.29
$NbCo_{1.05}Sn_{0.75}Sb_{0.25}$	5.9470(1)	8.5	-60	0.3	7.5	2.3	0.26
$NbCo_{1.05}Sn_{0.5}Sb_{0.5}$	5.9315(2)	8.3	-64	0.6	5.3	1.4	0.25
$NbCo_{1.05}Sb$	5.9028(1)	8.1	-68	0.3	6.9	2.5	0.33

Table 2. Lattice parameters (a), fractional site occupancies (Occ), thermal displacement parameters (U_{iso} / Å^2), weight percentages (wt%) of the phases present, and fit statistics for the $NbCo_{1+y}Sn$ (y = 0, 0.05) $Nb_{0.8}A_{0.2}CoSn$ (A = Ti, Zr) and $NbCo_{1.05}Sn_{1-z}Sb_z$ ($0 \leq z \leq 1$) samples from Rietveld fits against neutron powder diffraction data. Samples were sintered in Ta foil.

		$NbCoSn$	$NbCo_{1.05}Sn$	$Nb_{0.8}Ti_{0.2}Co_{1.05}Sn$	$Nb_{0.8}Zr_{0.2}CoSn$	$NbCo_{1.05}Sn_{0.75}Sb_{0.25}$	$NbCo_{1.05}Sn_{0.5}Sb_{0.5}$	$NbCo_{1.05}Sb$	$NbCoSb$
***a* (Å)**		5.9503(1)	5.9490(1)	5.9657(1)	HH 1- 5.9936(1) HH 2- 5.9607(2)	5.9418(1)	5.9278(1)	5.9006(1)	5.8978(1)
X	Occ	1.01(1)	1.00(1)	Nb – 0.87(1) Ti – 0.13(1)	Nb – 0.8 Zr – 0.2	0.97(1)	0.92(1)	0.86(1)	0.87(1)
	U_{iso}	0.0047(1)	0.0048(1)	0.0032(3)	0.0066(5)	0.0056(1)	0.0042(1)	0.0041(1)	0.0047(4)
Y1	Occ	1	1	1	1	1	1	1	1
	U_{iso}	0.0038(2)	0.0037(8)	0.0035(4)	0.0045(9)	0.0051(2)	0.0072(6)	0.0011(1)	0.0120(1)
Z	Occ	1	1	1	1	Sn 0.75 Sb 0.25	Sn 0.5 Sb 0.5	1	1
	U_{iso}	0.0023(8)	0.0022(7)	0.0056(6)	0.0028(7)	0.0027(1)	0.0069(8)	0.0108(7)	0.0135(2)
wt% Phases									
Main Phase		90.9(1)	97.5(9)	95.3(6)	HH 1 – 83.7(1) HH 2 – 16.3(1)	88.3(2)	91.8(2)	83.5(1)	72.8(1)
Impurities									
Nb_3Sn		7.2(1)	1.5(1)	-	-	-	-	-	-
Nb		1.9(1)	0.9(1)	-	-	1.1(1)	1.8(1)	-	-
Ti		-	-	4.7(1)	-	-	-	-	-
Nb_3Sb		-	-	-	-	2.9(1)	4.6(1)	9.8(1)	-
Co_7Nb_6		-	-	-	-	5.4(3)	-	-	-
CoSb		-	-	-	-	2.3(5)	-	-	-
Nb_5Sb_4		-	-	-	-	-	1.8(3)	6.7(3)	27.2(7)
Fit Statistics									
x^2		2.0	2.6	1.9	2.4	1.8	2.0	3.7	4.2
wR_p (%)									
	Bank 4	2.3	2.6	2.4	2.2	2.2	2.3	3.1	3.4
	Bank 5	2.3	2.4	2.3	2.4	2.2	2.1	3.2	3.4
R_p (%)									
	Bank 4	3.8	4.0	3.7	3.5	3.5	3.4	4.5	4.7
	Bank 5	3.3	3.6	3.4	3.9	3.2	3.2	4.6	4.8

Space group: $F\bar{4}3m$. Nb/Ti/Zr: (0,0,0) Co: (¼, ¼, ¼) Sn/Sb: (½, ½, ½).

View Article Online
DOI: 10.1039/C7CP07521A

Table 3. Lattice thermal conductivity at 323K (κ_{lat}), Nb-site vacancy fraction, calculated mass (Γ_M) and experimental (Γ_{exp}) disorder scattering parameters for the $NbCo_{1.05}Sn_{1-z}Sb_z$ ($0 \leq z \leq 1$) series.

z	$\kappa_{lat, 323K}$ (W m^{-1} K^{-1})	Nb-vacancies	Γ_M	Γ_{exp} [(a)]	
				κ_P = 9.8 W m^{-1} K^{-1}	κ_P = 8.1 W m^{-1} K^{-1}
0	9.8 / 8.1	0	0	0	0
0.1	6.9	0.01	0.01	0.02	0.01
0.25	5.3	0.03	0.02	0.04	0.03
0.5	4.1	0.08	0.06	0.08	0.07
1	4.9	0.14	0.09	0.07	0.04

[(a)] Γ_{exp} are calculated with respect to the κ_{lat} values for NbCoSn (κ_P = 9.8 W m^{-1} K^{-1}) and $NbCo_{1.05}Sn$ (κ_P = 8.1 W m^{-1} K^{-1}).

View Article Online
DOI: 10.1039/C7CP07521A

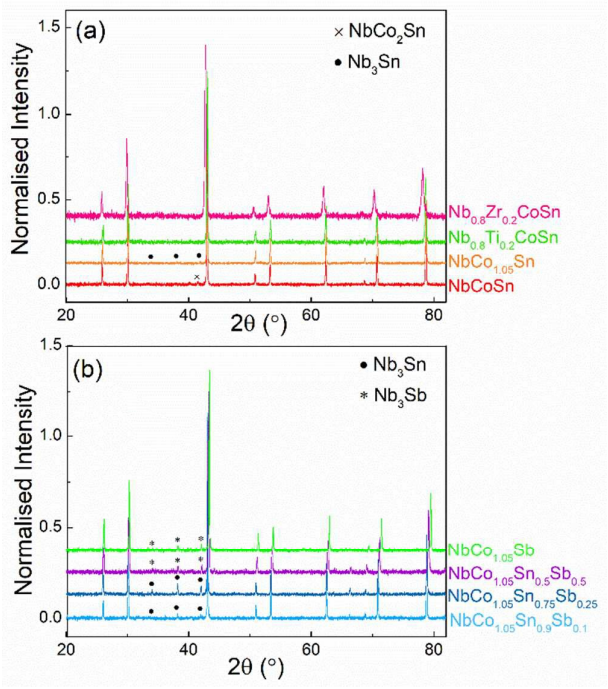

Figure 1: X-ray powder diffraction data for the **(a)** $NbCo_{1+y}Sn$ (y = 0, 0.05), $Nb_{0.8}A_{0.2}CoSn$ (A = Ti, Zr) and **(b)** $NbCo_{1.05}Sn_{1-z}Sb_z$ ($0 \leq z \leq 1$) samples after hot pressing. All samples were prepared by sintering in Nb foil.

View Article Online
DOI: 10.1039/C7CP07521A

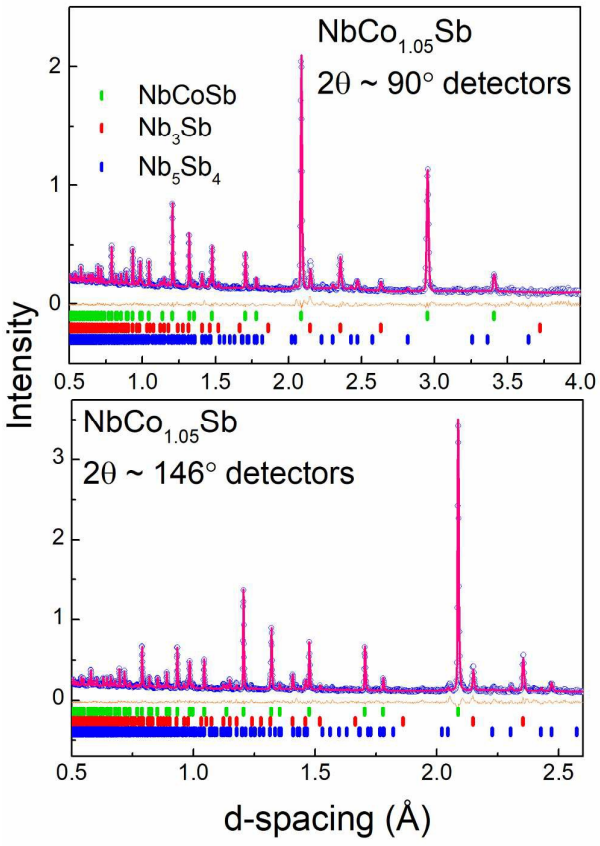

Figure 2: Fitted powder neutron diffraction profiles for $NbCo_{1.05}Sb$. Blue circles are observed data, red lines are calculated profile, orange lines are difference profiles (obs-calc). Vertical lines indicate Bragg reflection positions (phases indicated in figures).

View Article Online
DOI: 10.1039/C7CP07521A

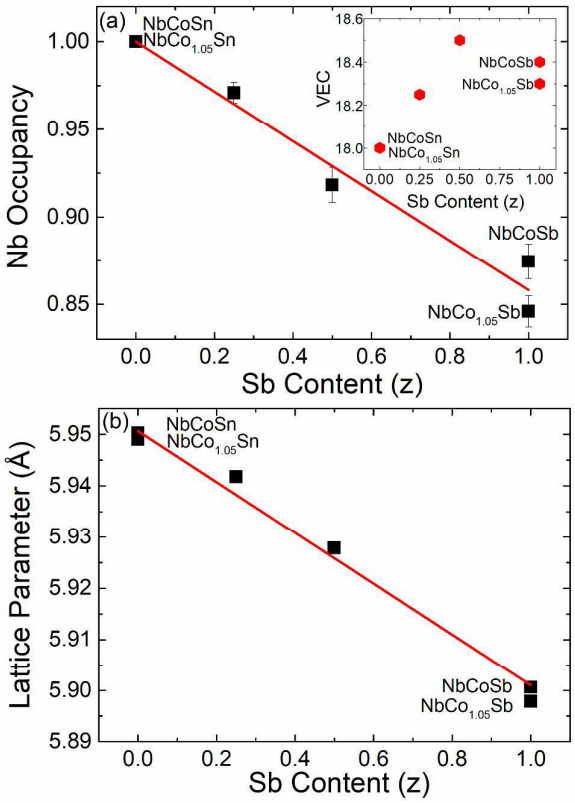

Figure 3: Composition dependence of **(a)** the Nb site occupancy and **(b)** lattice parameter for the $NbCo_{1.05}Sn_{1-z}Sb_z$ series ($0 \leq z \leq 1$) from Rietveld fits against neutron powder diffraction data. The inset to panel (a) shows the calculated valence electron count (VEC) based on the experimental compositions. Data for samples prepared using Ta foil.

View Article Online
DOI: 10.1039/C7CP07521A

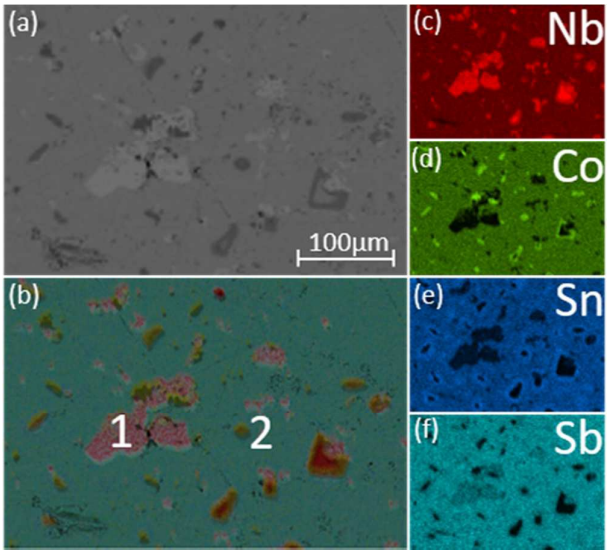

Figure 4: (a) Backscattered electron image SEM image, **(b)** layered EDX elemental map and **(c-f)** individual elemental maps for the $NbCo_{1.05}Sn_{0.5}Sb_{0.5}$ sample prepared using Nb foil. The HH matrix has an experimental $Nb_{0.93(1)}CoSn_{0.54(1)}Sb_{0.49(2)}$ composition. Regions labelled (1) and (2) are Nb_3Sb and Nb_6Co_7, respectively.

View Article Online
DOI: 10.1039/C7CP07521A

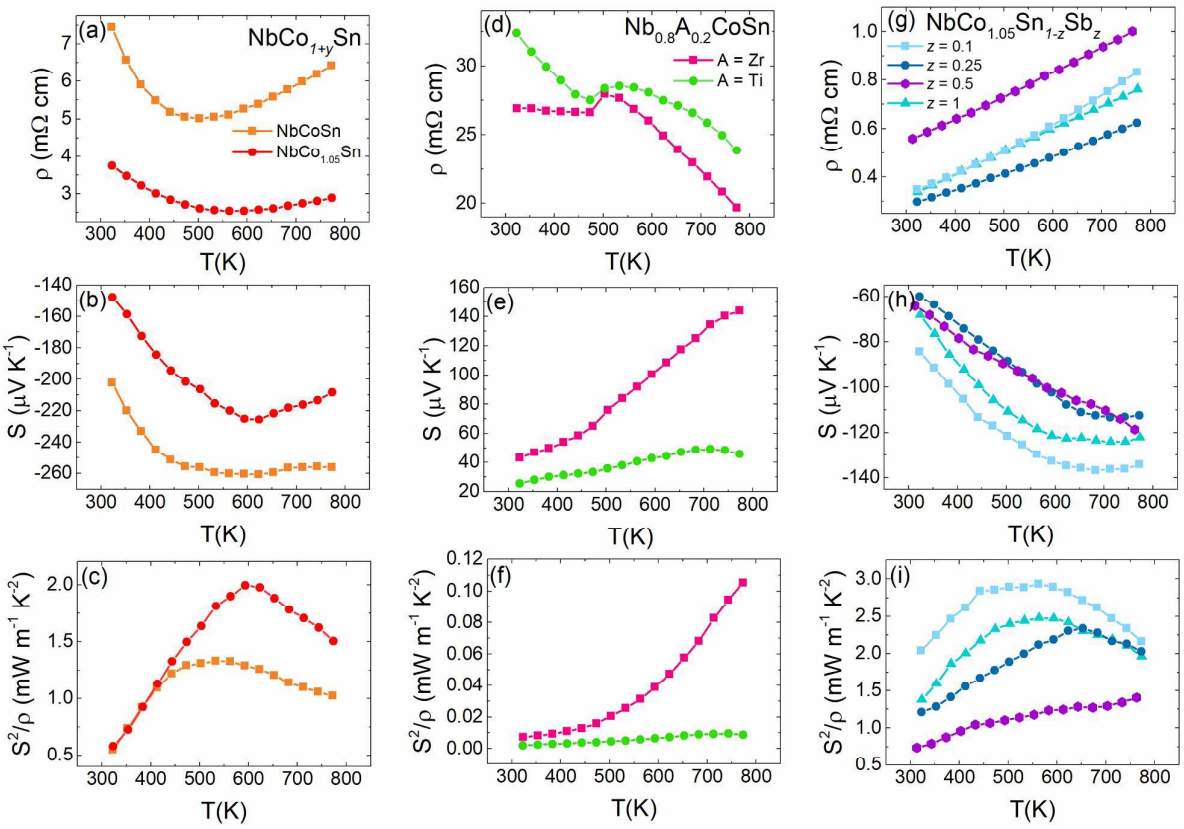

Figure 5: Temperature dependence of the electrical resistivity (ρ), Seebeck coefficient (S), and power factor (S^2/ρ) for the $NbCo_{1+y}Sn$ (y = 0, 0.05) **(a-c)**, $Nb_{0.8}A_{0.2}CoSn$ (A = Ti, Zr) **(d-f)** and $NbCo_{1.05}Sn_{1-z}Sb_z$ ($0 \leq z \leq 1$) samples **(g-i)**.

View Article Online
DOI: 10.1039/C7CP07521A

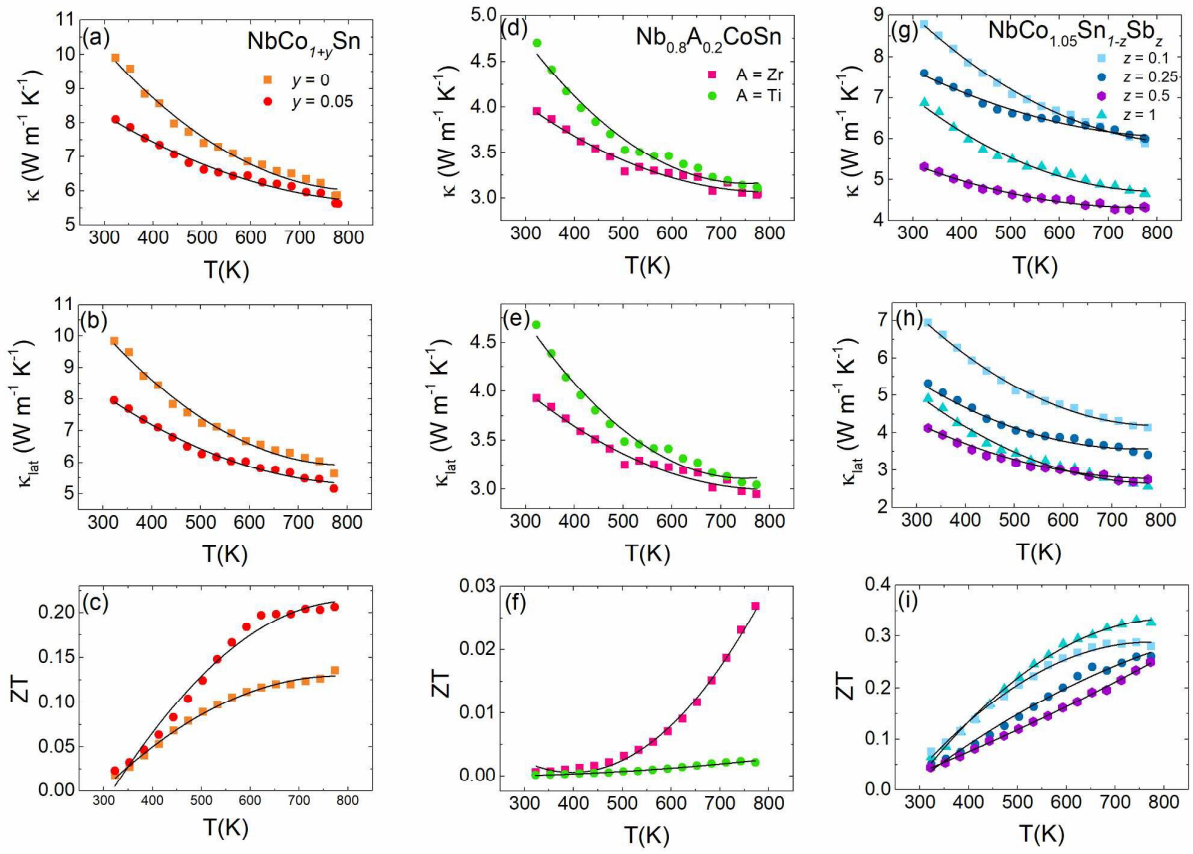

Figure 6: Temperature dependence of the total thermal conductivity (κ), lattice thermal conductivity (κ_{lat}) and ZT for the $NbCo_{1+y}Sn$ (y = 0, 0.05) **(a-c)**, $Nb_{0.8}A_{0.2}CoSn$ (A = Ti, Zr) **(d-f)** and $NbCo_{1.05}Sn_{1-z}Sb_z$ ($0 \leq z \leq 1$) samples **(g-i)**. Solid lines are guides to the eye.

View Article Online
DOI: 10.1039/C7CP07521A

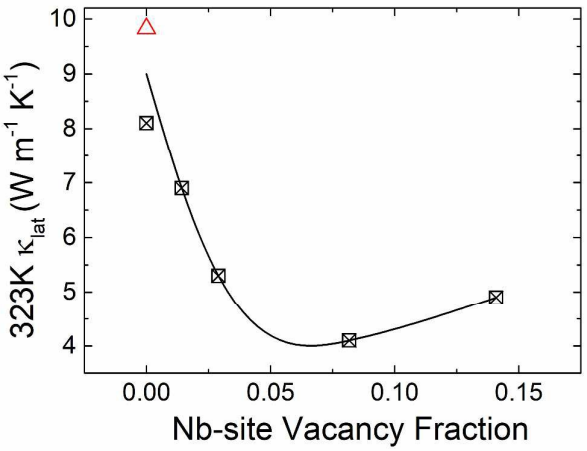

Figure 7: The 323 K lattice thermal conductivity (κ_{lat}) plotted against Nb deficiency for the $NbCo_{1.05}Sn_{1-z}Sb_z$ series, obtained from Rietveld analysis of neutron powder diffraction data. The red data point is for the NbCoSn sample prepared without excess Co. The solid line is a guide to the eye.

View Article Online
DOI: 10.1039/C7CP07521A

References

1. D. M. Rowe, ed., *Thermoelectrics and its Energy Harvesting*, CRC Press Boca Raton, 2012.
2. G. J. Snyder and E. S. Toberer, *Nat Mater*, 2008, **7**, 105-114.
3. S. Chen and Z. F. Ren, *Materials Today*, 2013, **16**, 387-395.
4. J. W. G. Bos and R. A. Downie, *J Phys-Condens Mat*, 2014, **26**, 433201.
5. T. J. Zhu, C. G. Fu, H. H. Xie, Y. T. Liu and X. B. Zhao, *Adv Energy Mater*, 2015, **5**, 1500588.
6. L. Chen, X. Y. Zeng, T. M. Tritt and S. J. Poon, *Journal of Electronic Materials*, 2016, **45**, 5554-5560.
7. S. Populoh, M. H. Aguirre, O. C. Brunko, K. Galazka, Y. Lu and A. Weidenkaff, *Scripta Materialia*, 2012, **66**, 1073-1076.
8. M. Schwall and B. Balke, *Physical Chemistry Chemical Physics*, 2013, **15**, 1868-1872.
9. R. A. Downie, D. A. MacLaren and J. W. G. Bos, *Journal of Materials Chemistry A*, 2014, **2**, 6107-6114.
10. G. Joshi, X. Yan, H. Z. Wang, W. S. Liu, G. Chen and Z. F. Ren, *Adv Energy Mater*, 2011, **1**, 643-647.
11. X. A. Yan, G. Joshi, W. S. Liu, Y. C. Lan, H. Wang, S. Lee, J. W. Simonson, S. J. Poon, T. M. Tritt, G. Chen and Z. F. Ren, *Nano Lett*, 2011, **11**, 556-560.
12. J. P. A. Makongo, D. K. Misra, X. Y. Zhou, A. Pant, M. R. Shabetai, X. L. Su, C. Uher, K. L. Stokes and P. F. P. Poudeu, *Journal of the American Chemical Society*, 2011, **133**, 18843-18852.
13. Y. F. Liu, P. Sahoo, J. P. A. Makongo, X. Y. Zhou, S. J. Kim, H. Chi, C. Uher, X. Q. Pan and P. F. P. Poudeu, *Journal of the American Chemical Society*, 2013, **135**, 7486-7495.
14. R. A. Downie, R. I. Smith, D. A. MacLaren and J. W. G. Bos, *Chemistry of Materials*, 2015, **27**, 2449-2459.
15. C. Yu, T. J. Zhu, R. Z. Shi, Y. Zhang, X. B. Zhao and J. He, *Acta Materialia*, 2009, **57**, 2757-2764.
16. R. A. Downie, D. A. MacLaren, R. I. Smith and J. W. G. Bos, *Chemical Communications*, 2013, **49**, 4184-4186.
17. L. Chen, S. Gao, X. Zeng, A. M. Dehkordi, T. M. Tritt and S. J. Poon, *Appl Phys Lett*, 2015, **107**, 041902.
18. M. Gurth, G. Rogl, V. V. Romaka, A. Grytsiv, E. Bauer and P. Rogl, *Acta Materialia*, 2016, **104**, 210-222.
19. C. Fu, T. Zhu, Y. Liu, H. Xie and X. Zhao, *Energy & Environmental Science*, 2015, **8**, 216-220.
20. C. G. Fu, S. Q. Bai, Y. T. Liu, Y. S. Tang, L. D. Chen, X. B. Zhao and T. J. Zhu, *Nature Communications*, 2015, **6**.
21. E. Rausch, B. Balke, J. M. Stahlhofen, S. Ouardi, U. Burkhardt and C. Felser, *Journal of Materials Chemistry C*, 2015, **3**, 10409-10414.
22. R. He, L. H. Huang, Y. M. Wang, G. Samsonidze, B. Kozinsky, Q. Y. Zhang and Z. F. Ren, *APL Materials*, 2016, **4**, 104804.
23. Y. Ono, S. Inayama, H. Adachi and T. Kajitani, *Jpn J Appl Phys 1*, 2006, **45**, 8740-8743.
24. Y. Ono, S. Inayama, S. Yotasuhashi, H. Adachi, Y. Miyazaki and T. Kahitani, *Transactions of the Materials Research Society of Japan*, 2004, **29**, 2785-2788.
25. Y. Kimura, Y. Tamura and T. Kita, *Appl Phys Lett*, 2008, **92**.
26. Y. Kawaharada, K. Kurosaki, H. Muta, M. Uno and S. Yamanaka, *Journal of Alloys and Compounds*, 2004, **384**, 303-307.
27. Y. Kawaharada, K. Kurosaki, H. Muta, M. Uno and S. Yamanaka, *Journal of Alloys and Compounds*, 2004, **377**, 312-315.

View Article Online
DOI: 10.1039/C7CP07521A

28. S. Bhattacharya and G. K. H. Madsen, *Journal of Materials Chemistry C*, 2016, **4**, 11261-11268.
29. M. L. C. Buffon, G. Laurita, N. Verma, L. Lamontagne, L. Ghadbeigi, D. L. Lloyd, T. D. Sparks, T. M. Pollock and R. Seshadri, *J Appl Phys*, 2016, **120**, 075104.
30. L. H. Huang, R. He, S. Chen, H. Zhang, K. Dahal, H. Q. Zhou, H. Wang, Q. Y. Zhang and Z. F. Ren, *Mater Res Bull*, 2015, **70**, 773-778.
31. W. G. Zeier, S. Anand, L. H. Huang, R. He, H. Zhang, Z. F. Ren, C. Wolverton and G. J. Snyder, *Chemistry of Materials*, 2017, **29**, 1210-1217.
32. A. C. Larson and R. B. Von Dreele, *General Structure Analysis System (GSAS)*, Los Alamos National Laboratory Report LAUR 86-748, 2000.
33. B. H. Toby, *Journal of Applied Crystallography*, 2001, **34**, 210-213.
34. R. A. Downie, S. A. Barczak, R. I. Smith and J. W. G. Bos, *Journal of Materials Chemistry C*, 2015, **3**, 10534-10542.
35. Tables of Physical & Chemical Constants (16th edition 1995). 3.7.5 Atomic radii. Kaye & Laby Online Version 1.0 (2005) www.kayelaby.npl.co.uk.
36. E. S. Toberer, A. Zevalkink and G. J. Snyder, *Journal of Materials Chemistry*, 2011, **21**, 15843-15852.
37. J. Callaway, *Physical Review*, 1959, **113**, 1046-1051.
38. J. Yang, G. P. Meisner and L. Chen, *Appl Phys Lett*, 2004, **85**, 1140-1142.
39. B. C. Sales, B. C. Chakoumakos, D. Mandrus and J. W. Sharp, *Journal of Solid State Chemistry*, 1999, **146**, 528-532.